



Surface hydroxyl group-enriched nickel cobalt molybdate hydrate for improved oxygen evolution activity in an anion exchange membrane water electrolyzer



Ayon Karmakar ^a, Thillai Govindaraja Senthamarai Kannan ^b, Erdenebayar Baasanjav ^a, Parthasarathi Bandyopadhyay ^a, Bo Jin ^d, Yoo Sei Park ^{c,*}, Dong-Hee Lim ^{b,*}, Sang Mun Jeong ^{a,*}

^a Department of Chemical Engineering, Chungbuk National University, 1 Chungdae-ro, Seowon-Gu, Cheongju, Chungbuk 28644, Republic of Korea

^b Department of Environmental Engineering, Chungbuk National University, 1 Chungdae-ro, Seowon-Gu, Cheongju, Chungbuk 28644, Republic of Korea

^c Department of Advanced Material Engineering, Chungbuk National University, 1 Chungdae-ro, Seowon-gu, Cheongju, Chungbuk 28644, Republic of Korea

^d Key Laboratory of Automobile Materials, Ministry of Education, and College of Materials Science and Engineering, Jilin University, Changchun 130022, China

ARTICLE INFO

Keywords:

Nickel cobalt molybdate hydrates
Surface hydroxyl groups, gram scale synthesis
Synergistic effect
Oxygen evolution reaction
Anion exchange membrane water electrolyzer

ABSTRACT

The present report depicts a simple one-step reflux method to fabricate nickel cobalt molybdate hydrate (NCMH) nanostructured rods in gram-scale ($>1.8\text{ g}$). The structure and electrocatalytic oxygen evolution reaction (OER) activity of the NCMH have been explored both experimentally and theoretically. Further, experimental and theoretical analyses indicate that the presence of cobalt in NCMH promotes OH adsorption and enrichment of the NCMH surface with hydroxyl functionalities, which in turn improves the interfacial electrochemistry of NCMH to display better alkaline OER performance than either nickel molybdate hydrate or cobalt molybdate hydrate. In addition, the single cell anion exchange membrane (AEM) water electrolyzer containing an NCMH anode outperforms the commercial IrO_2 anode with high current density of $\sim 1.0\text{ A cm}^{-2}$ at $1.82\text{ V}_{\text{cell}}$ and stable performance for 58 h with $\sim 74.57\%$ cell efficiency. Therefore, nickel cobalt molybdenum oxide hydrate nanorods can serve as promising anode materials for AEM water electrolyzers.

1. Introduction

The search for clean, reliable, and affordable energy sources has been the primary goal of the human race since the beginning of the industrial revolution, as fossil fuels are being depleted at an exponential rate. [1–3] Hydrogen is one of the most clean and important alternatives to the conventional energy resources. [4,5] In this regard, water electrolyzers have emerged as promising and environment-friendly systems for the production of hydrogen towards the sustainable hydrogen fuel economy. [6–8] However, the higher overpotential and slower reaction rate of the oxygen evolution reaction (OER) than those of the hydrogen evolution reaction (HER), make OER the most critical step for electrocatalytic water splitting. [9,10] In order to catalyze the OER, effective and stable electrocatalysts are essential for long-term applications. Therefore, the advancement of effective and durable electrode materials for water electrolysis is of immense interest.

Ru- and Ir-based materials, such as Ru/C , RuO_2 , Ir/C , and IrO_2 , are well known benchmark OER electrocatalysts. [11] Nonetheless, the high

cost and low abundance of Ru- and Ir-based materials have limited their large-scale applications in OER. [12] Therefore, earth-abundant and cost-effective transition metal oxides with desirable properties have attracted considerable attention. [5] In view of this, transition metal molybdates have garnered significant interest as electrode materials in electrocatalytic applications. [13–15] For instance, Wang et al. [16] studied the morphology-dependent OER activity of $\text{NiMoO}_4 \cdot \text{H}_2\text{O}$ nanostructures prepared by using a temperature-controlled hydrothermal technique and found that one-dimensional (1D) nanorods were superior to two-dimensional (2D) nanosheets. In another OER study, NiMoO_4 nanorods, fabricated through a hydrothermal reaction followed by calcination in air, exhibited overpotential value of 340 mV to reach a geometric current density of 10 mA cm^{-2} in alkaline media. This material also surpassed its monometallic counterparts NiO and MoO_3 . Notably, the incorporation of Mo facilitated the oxidation of Ni^{2+} in electrocatalytically active Ni^{3+} . [17] The three-dimensional (3D) oxygen deficient CoMoO_4 nanodimensional sheets on Ni foam exhibited ~ 295 mV overpotential at 10 mA cm^{-2} . [18] It was speculated that the

* Corresponding authors.

E-mail addresses: yspark@chungbuk.ac.kr (Y.S. Park), limkr@cbnu.ac.kr (D.-H. Lim), smjeong@chungbuk.ac.kr (S.M. Jeong).

oxygen vacancies facilitated the OER kinetics by lowering the water adsorption energy on the CoMoO_4 surface. Guan et al. [19] reported a Pt-modified Ni-Mo-based material with an OER overpotential of 399 mV at 50 mA cm⁻², noting the positive influence of oxygen vacancies on the charge transfer kinetics due to Pt incorporation and annealing. In addition, mixed transition metal molybdates have also been reported to display higher electrochemical activity owing to their variable oxidation states, rich redox properties, and enhanced electrical conductivity. [20, 21] For example, the mixed metal molybdate, composed of $\text{CoMoO}_4\text{-NiMoO}_4$ nanotubes with an optimized composition, was found to exhibit superior OER output to that of the individual components, resulting in a low overpotential (~ 300 mV at 10 mA cm⁻²) in 1 M aqueous KOH. [22] While monometallic or mixed molybdates in anhydrous form are mostly investigated for electrocatalytic applications, it should be noted that mixed NiCo molybdate hydrates have rarely been explored as electrode materials for water electrolysis. On the other hand, most preparatory methods for the synthesis of mixed or singular metal molybdates include multiple steps, post-thermal treatments, and expensive solvents, making them neither economical nor energy efficient. [14,15,23,24] Thus, simple, one-step, and scalable fabrication of single-phase NiCo molybdate hydrates is highly desirable. Furthermore, the interfacial interaction of hydroxide ions/water molecules with the catalyst surface is crucial for determining the fate of anodic OER. [25] As an example, Chen et al. [26] noted enhanced stability of surface hydroxyl species owing to the introduction of Ni in CoOOH , which resulted in a rapid charge transfer kinetics at the interface. Therefore, identifying the role of surface hydroxyl functionalities is important for developing effective electrocatalysts.

Anion-exchange membrane (AEM) water electrolysis is a reliable technology for a low-cost and sustainable hydrogen economy. The AEM water electrolyzer utilizes both the low capital cost of alkaline water electrolyzer (AWE) and high operational behavior/performance of proton exchange membrane water electrolyzer (PEMWE) with high-pressure hydrogen generation by using platinum group metal (PGM)-free electrode components and a membrane electrode assembly (MEA) with a zero-gap configuration. [27,28] In general, the catalyst-coated substrate (CCS) method is used to fabricate the catalyst layer of MEAs in commercial water electrolyzers, requiring large amounts of powdered materials. [6,29] The products prepared by using complex/multistep procedures in the laboratory are usually on the milligram scale, which is insufficient for MEA fabrication. This can be addressed by employing scalable or gram-scale synthesis of powdered materials through a one-step reflux technique.

Motivated by these findings, the current study is focused on the facile cost-effective gram-scale fabrication of NiCo molybdate hydrates ($\text{Ni}_{0.5}\text{Co}_{0.5}\text{MoO}_4\bullet\text{nH}_2\text{O}$) using a simple one-step reflux method in aqueous media. We investigated the effect of Co introduced to a Ni molybdate hydrate to a Ni molybdate hydrate and how the electrocatalytic OER performance is affected. Subsequent physicochemical characterizations led to comparisons of $\text{Ni}_{0.5}\text{Co}_{0.5}\text{MoO}_4\bullet\text{nH}_2\text{O}$ (referred to as NCMH) with nickel molybdate hydrate (NMH) and cobalt molybdate hydrate (CMH). Experimental investigations and first-principles density functional theory (DFT) calculations were employed to ascertain the impact of Co incorporation in hydrous NiMoO_4 on OH adsorption and enrichment of the surface with hydroxyl functionalities. Moreover, electrochemical studies to assess alkaline OER activity and durability of NCMH in a three-electrode configuration and comparison of an NCMH-based anode with a commercial IrO_2 anode in a full-cell AEM water electrolyzer device are presented.

2. Experimental

2.1. Fabrication of nickel cobalt molybdate hydrate

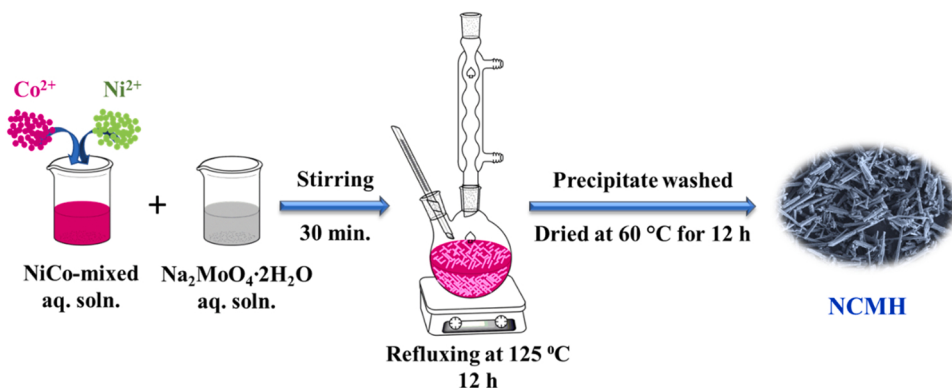
In a simple procedure, 0.1 M 50 mL aqueous solution each of $\text{NiCl}_2\bullet 6\text{H}_2\text{O}$ and $\text{CoCl}_2\bullet 6\text{H}_2\text{O}$ (molar ratio 1:1) were mixed together with and

30 min stirring. In another beaker, 0.1 M 100 mL aqueous solution of $\text{Na}_2\text{MoO}_4\bullet 2\text{H}_2\text{O}$ was prepared. This solution was added drop-by-drop to the previously prepared NiCo-mixed solution under constant stirring for 30 min. Subsequently, the resultant solution was transferred to a 500 mL round-bottomed flask equipped with a condenser and refluxed in a preheated (125 °C) oil bath for 12 h. After the bath temperature reached to 25 °C, the obtained precipitate underwent successive washing with water/ethanol, followed by drying in an electric vacuum oven at 60 °C for 12 h. The powdered product ($\sim 1.84 \pm 0.02$ g) was identified as NCMH. Nickel molybdate hydrate ($\text{NiMoO}_4\bullet\text{nH}_2\text{O}$) and cobalt molybdate hydrate ($\text{CoMoO}_4\bullet\text{nH}_2\text{O}$) were also prepared for comparison under identical conditions, referred to as NMH and CMH, respectively. In addition, anhydrous nickel cobalt molybdate (NCMO) was fabricated by annealing the NCMH at 450 °C for 2 h in an Ar-atmosphere.

3. Results and discussion

3.1. Physicochemical Characterizations

The nickel cobalt molybdate hydrate (NCMH) nanostructured rods were fabricated using a one-step reflux method and illustrated in Scheme 1. Initially, aqueous solutions of $\text{Ni}(\text{NO}_3)_6\text{H}_2\text{O}$ and $\text{Co}(\text{NO}_3)_6\text{H}_2\text{O}$ were mixed together at room temperature, forming a mixed aqueous solution of Ni and Co. This mixed solution was not refluxed prior to the addition of aqueous $\text{Na}_2\text{MoO}_4\bullet 2\text{H}_2\text{O}$ solution. Subsequently, reflux reaction of the total aqueous solution of reactants was carried out after adding aqueous $\text{Na}_2\text{MoO}_4\bullet 2\text{H}_2\text{O}$ solution to the previously prepared NiCo aqueous solution to form NCMH. Notably, the proposed fabrication procedure is scalable, as > 1.8 g product (NCMH) can be obtained from a single reaction. The crystallinity of NCMH was characterized by X-ray diffractometry (XRD) and compared with that of NMH. Fig. 1a shows that the XRD pattern of NMH matched well with the triclinic phase of $\text{NiMoO}_4\bullet 0.75\text{H}_2\text{O}$ (ICDD no. 04-017-0338). [30] The diffraction peaks of NCMH were in good agreement with those of NMH, and could be indexed to the (001), (100), (111), (121), (003), (103), (122), (104), and (141) planes. Further, the XRD pattern of CMH (Fig. S2a) was in accordance with the triclinic $\text{CoMoO}_4\bullet 0.75\text{H}_2\text{O}$ (ICDD no. 04-011-8282). [31] Notably, the peak positions of NMH and CMH are quite close according to the standard ICDD patterns (Fig. S3). As a result, it is hard to find separate peaks of NMH and CMH in NCMH. In addition, almost similar crystal radius of Ni^{2+} (0.069 nm) and Co^{2+} (0.072 nm) was found to be beneficial in preparing single phase solid-solution. [32,33] These findings clearly demonstrate that the incorporation of Co into NMH did not alter the crystal structure and single phase triclinic NiCo molybdate hydrates was formed. Moreover, Fig. 1b shows a shift of the (121) and (003) peak positions to lower 2θ values in NCMH with respect to NMH, with no splitting of these peaks observed. These findings reaffirmed the successful incorporation of Co into the Ni molybdate hydrate crystal lattice and the formation of a single phase NCMH. No additional peaks of NiCo-based hydroxides/-oxides were observed in the XRD of NCMH as aqueous solutions of Ni and Co-salts were mixed together at room temperature in the first step of preparation procedure, which didn't undergo any refluxing prior to the addition of aqueous solution of MoO_4^{2-} . Thus, the absence of any other impurity peaks indicates the presence of highly phase-pure mixed metal molybdate hydrates. Furthermore, the bulk structures of NMH, NCMH, and CMH were theoretically optimized on the basis of ICDD no. 04-017-0338 and are displayed in Figs. 1c, 1d, and S2b, respectively. The findings indicated the presence of four Mo and sixteen O in common along with four Ni for NMH, four Co for CMH, and two Ni and two Co for NCMH with the triclinic lattice parameters of $a = 6.779 \text{ \AA}$, $b = 6.890 \text{ \AA}$, $c = 9.249 \text{ \AA}$, $\alpha = 76.681^\circ$, $\beta = 83.960^\circ$, and $\gamma = 74.218^\circ$. These results matched well with the experimentally prepared triclinic form of the hydrated nickel molybdate and cobalt molybdate structures. [30] The relatively poor crystallization of NCMH can also be ascertained from the



Scheme 1. Illustration of the preparation procedure for NCMH.

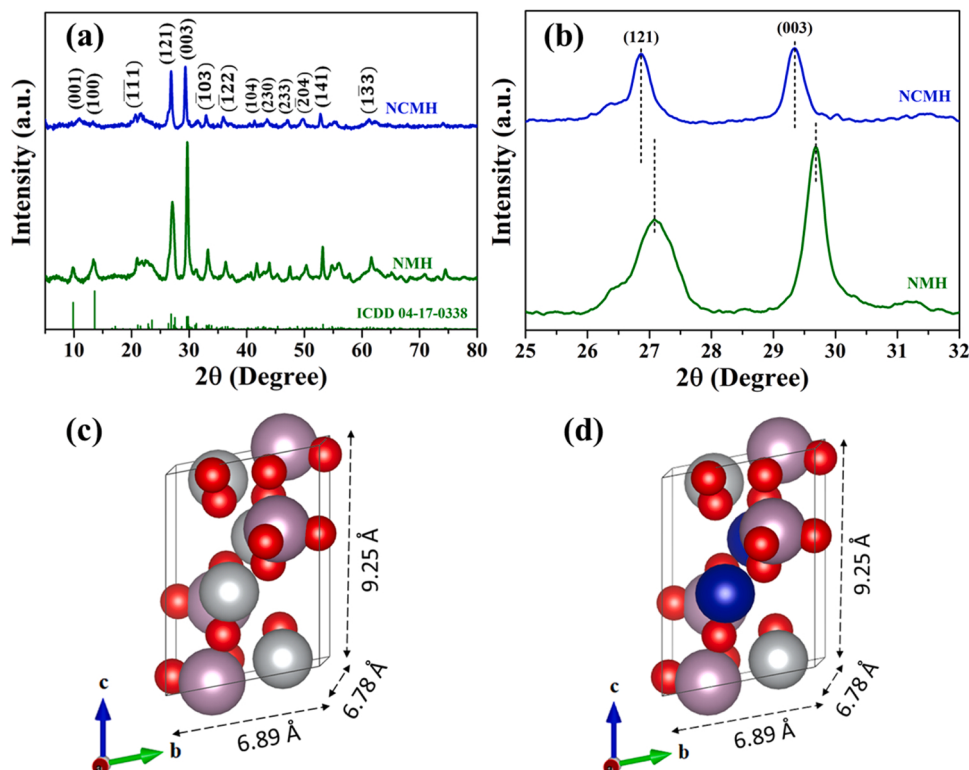


Fig. 1. (a) X-ray diffractograms and (b) enlarged (121) and (003) peak positions of NMH and NCMH. Triclinic (c) NMH and (d) NCMH bulk structures (atom colors: Mo = pink, Ni = grey, Co = blue, and O = red).

reduced intensity of the diffraction peaks compared to that of NMH. The lower crystallinity indicates presence of amorphous components and more defect sites in NCMH, which are usually considered as the catalytically active sites that enhance the electrocatalytic performances. [22] Notably, Anantharaj et al. [34] indicated the advantage of low crystalline structure in facilitating the electrolyte diffusion owing to the flexibility of disordered structural units, leading to larger electrode-electrolyte interface. Thus, in all probability, NCMH contains more transportation channels for electrolyte diffusion that are beneficial for improving electrochemical performance owing to its more amorphous character than NMH. [35].

Fourier-transform infrared (FTIR) spectroscopy analysis of NMH and NCMH was performed to obtain information about the relative amount of surface hydroxyl groups. The corresponding spectra of NMH and NCMH in the range of 4000–400 cm^{-1} are shown in Fig. S4. The appearance of the broad signals in the range of 3600–3000 cm^{-1} were ascribed to the hydroxyl group (O-H) stretching vibration. [36] The

relative intensity and area under the OH peak were greater for NCMH than NMH, thus indicating the presence of more OH functionalities on NCMH. [37] Further, the peak located at $\sim 1623 \text{ cm}^{-1}$ for all the samples was corresponding to O-H bending vibrations of $\delta_{\text{H}_2\text{O}}$ molecules. [36] The Mo-O stretching vibrations were appeared within the region of 970–740 cm^{-1} . [38] Further, the sharp peaks at ~ 960 and 743 cm^{-1} were attributed to the activation of ν_1 and ν_3 vibrational modes of distorted tetrahedral MoO_4 units. [39] Another peak at $\sim 439 \text{ cm}^{-1}$ in the spectra corresponds to the vibrations of M-O and Mo building blocks present in $\text{MMoO}_4 \bullet n\text{H}_2\text{O}$ ($\text{M} = \text{Ni, Co}$). [39] These findings clearly establish successful formation of hydrous nickel cobalt molybdate.

The morphology of the prepared samples was analyzed by field-emission scanning electron microscopy (FESEM) and corresponding findings are presented in Fig. 2(a, b, c). The formation of a 1D rod-like morphology was observed in all three samples. The high-magnification FESEM images in the insets of Fig. 2(a, b, c) clearly show the intermediate diameter of the NCMH nanostructured rods

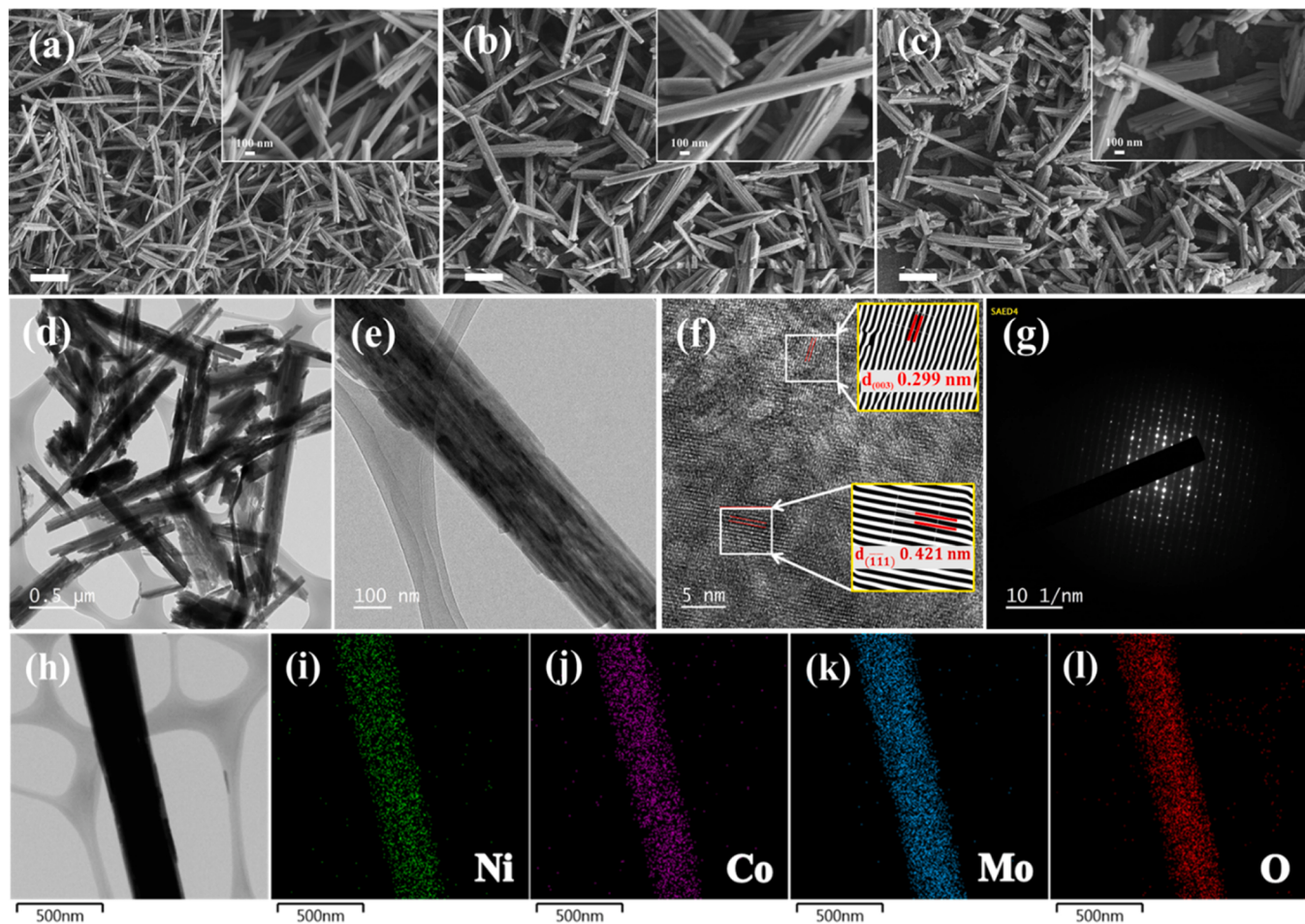


Fig. 2. Low magnification FESEM images (high magnification at insets) of (a) NMH, (b) CMH, and (c) NCMH. (d) Low and (e) high magnification TEM images, (f) HRTEM image, and (g) SAED pattern of NCMH. (h) HAADF-STEM image and (i–l) EDX elemental mapping of NCMH.

compared to NMH and CMH. The average diameter of the NMH, CMH, and NCMH nanostructured rods were found to be ~46.26, 173.09, and 57.4 nm, respectively (Fig. S5). In all probability, the intermediate diameter of NCMH can be accounted for by the coexistence of Ni^{2+} with Co^{2+} in NCMH. Park et al. [40] also observed similar findings for $\text{Ni}_{x}\text{Co}_{1-x}\text{MoO}_4$ nanorods prepared by the hydrothermal method. Thus, the synergistic effect of Ni^{2+} and Co^{2+} influences the size of NCMH. In addition, the transmission electron microscopy (TEM) images (low- and high-magnification) of NCMH (Fig. 2d and e) clearly show the growth of self-assembled tiny nanorods on its surface. Such self-assembly of nanorod units can be attributed to the presence of strong attractive forces due to the high surface energy of nanostructured units. [40] Fig. 2g represents the selected area electron diffraction (SAED) pattern of NCMH. The spot pattern in the SAED pattern is indicative of the formation of crystalline nanostructured rods of NCMH. Furthermore, the high-resolution TEM (HRTEM) image of NCMH (Fig. 2f) demonstrates the growth of lattice fringes with inter-planar distances of ~0.299 and 0.421 nm, related to the (003) and (111) planes, respectively. The energy-dispersive X-ray (EDX) spectrum of NCMH (Fig. S6) indicated an atomic ratio for Ni:Co:Mo of ~0.52:0.52:1, establishing the formation of $\text{Ni}_{0.5}\text{Co}_{0.5}\text{MoO}_4\bullet\text{nH}_2\text{O}$. Furthermore, the presence of Ni, Co, Mo, and O in NCMH was evident from the EDX elemental mapping, as shown in Fig. 2(i–l).

The surface elemental compositions of NCMH were deduced by X-ray photoelectron spectroscopy (XPS) and compared with those of NMH. Ni, Mo, and O were observed in the survey spectra (Fig. 3a) of NMH and NCMH. In addition, the XPS survey of NCMH indicated the presence of Co. Fig. 3b shows the Co 2p high-resolution spectrum of NCMH,

consisting of two spin-orbit peaks appeared at 797.0 eV (Co 2p_{1/2}) and 780.7 eV (Co 2p_{3/2}). [41] Further, the deconvoluted Co 2p_{1/2} and 2p_{3/2} peaks indicate the existence of both Co^{2+} and Co^{3+} . [42] The Co²⁺/Co³⁺ atomic ratios of the deconvoluted Co 2p_{1/2} (~1.43) and Co 2p_{3/2} (~2.04) peaks suggest that Co^{2+} is the dominant species in NCMH. The Ni 2p_{1/2} and 2p_{3/2} peaks appeared at ~873.3 and 855.5 eV, respectively, along with two shake-up satellites in the Ni 2p spectrum (Fig. 3c) of NMH. The presence of Ni^{3+} and Ni^{2+} was also evidenced by the respective deconvoluted Ni 2p_{1/2} (873.1 and 875.2 eV) and Ni 2p_{3/2} (857.3 and 855.5 eV) peaks. [19] The presence of Ni^{2+} as the major oxidation state in NMH was deduced from the ratio of the peak areas of Ni^{2+} and Ni^{3+} . The Ni 2p high-resolution XPS spectrum of NCMH showed chemical characteristics similar to those of NMH, except that the Ni 2p_{1/2} and Ni 2p_{3/2} peaks were shifted to higher binding energies. This could be ascribed to modifications of the electronic structure of NCMH due to the incorporation of Co in NMH. [43,44] The Mo 3d spectra of NMH and NCMH (Fig. 3d) exhibited two photoelectron peaks relating to Mo 3d_{3/2} and Mo 3d_{5/2}. [45] The spin-orbit splitting of ~3.2 eV between the 3d_{3/2} and 3d_{5/2} peaks of Mo indicated the +6 oxidation state of Mo in NMH and NCMH. [46] Further, the Mo 3d_{3/2} and 3d_{5/2} peaks in NCMH were blue-shifted by ~0.4 eV. It is known that high-valent Mo⁶⁺ species facilitate the oxidation of Ni^{2+} and Co^{2+} ions by an electron withdrawing effect. [41] As a result, higher oxidation states of Ni and Co will favor OH adsorption on the electrode surface in alkaline media. [47] Additionally, high-valence metal centers serve as the active sites in alkaline water electrolysis and are beneficial for achieving improved electrocatalytic activity. [48].

The O 1 s spectrum consisted of three peaks, corresponding to the

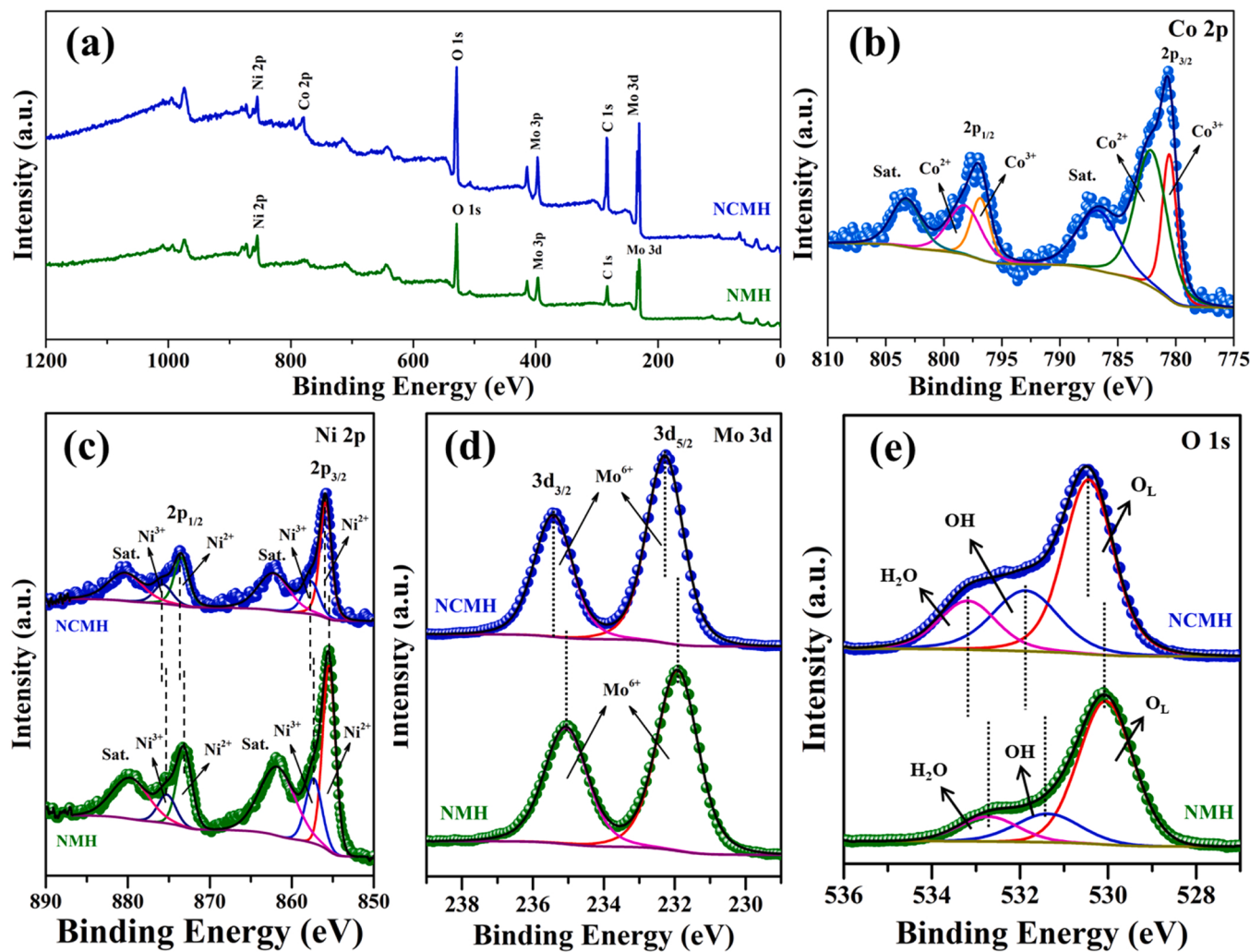


Fig. 3. (a) XPS survey scans of NMH and NCMH. (b) High resolution Co 2p spectrum of NCMH. The deconvoluted high-resolution spectra of (c) Ni 2p, (d) Mo 3d, and (e) O 1 s regions of NMH and NCMH.

crystalline water molecules (532.7 eV), hydroxyl groups (531.4 eV), and lattice oxygen (530.0 eV) present in NMH (Fig. 3e). [19,49] For NCMH, the O 1 s peaks were blue-shifted and an increase in the amount of -OH was also observed, as indicated by the larger peak area (~2.29 times larger than that of NMH). Additionally, the lattice oxygen content decreased from 70% in NMH to 56% in NCMH. These findings suggest an enrichment of NCMH with surface hydroxyl groups in the presence of Co compared to that of NMH. Notably, previous studies have indicated the positive influence of surface hydroxyl groups on the electrocatalytic OER. [25,26] Therefore, an increase in the concentration of surface -OH could be beneficial for boosting the OER performance of NCMH. The improved hydrophilicity of the NCMH surface was also expected based on this observation, which was further confirmed by contact angle measurements (Fig. S7). NCMH exhibited a low contact angle (9.02°) with the water droplet, indicating a more hydrophilic and aerophobic surface than that of NMH (13.14°).

3.2. Electrocatalytic Oxygen Evolution Activity in Three-Electrode Configuration

The electrocatalytic water oxidation or OER performances of NMH, CMH, and NCMH were investigated in a 1 M KOH electrolyte using a standard three-electrode cell, which consists of a platinum plate as counter, Ag/AgCl (KCl saturated) as reference, and sample-coated carbon fiber paper (CFP; current collector) as working electrodes. To

ascertain the influence of crystalline water molecules, the OER activity of anhydrous NCMO was also compared with that of NCMH (Fig. 4a-d). The η values at 10 and 50 mA cm⁻² current densities for NMH, CMH, NCMH, and NCMO were calculated from the iR -corrected LSV plots (scan rate: 5 mV s⁻¹), as presented in Fig. 4a. In addition, the polarization curves with and without iR -correction for NMH, CMH, NCMH, NCMO, and CFP are shown in Fig. S8. NCMH displayed a lower η_{10} value (~291 mV) than those of NMH (298 mV), CMH (344 mV), and NCMO (322 mV). Notably, NMH exhibited a slightly larger η_{10} than that of NCMH in the low-potential region. However, in the higher overpotential region, its OER performance deteriorated and appeared to be inferior to that of CMH after 1.639 V vs. RHE. This clearly indicates that NMH is not suitable for high-current water oxidation applications. Furthermore, the difference in overpotential (η_{50}) between NMH and NCMH was evident at a high current density (50 mA cm⁻²). Notably, lower OER overpotentials of NCMH than that of anhydrous NCMO at all current densities confirmed the superiority of hydrated mixed metal molybdate over the anhydrous one. This finding further reaffirms our earlier speculation on the hydroxyl rich surface of hydrated catalyst to provide more active sites and higher OER activity. Thus, NCMH was found to be the best-performing electrode material for the OER among the prepared samples. The improved OER performance of NCMH can be attributed to the synergistic interaction between Ni²⁺ and Co²⁺ present in NCMH. Furthermore, the η_{10} value of NCMH is similar to that of commercial RuO₂ (290 mV @ 10 mA cm⁻²). [50] Additionally, NCMH outperforms

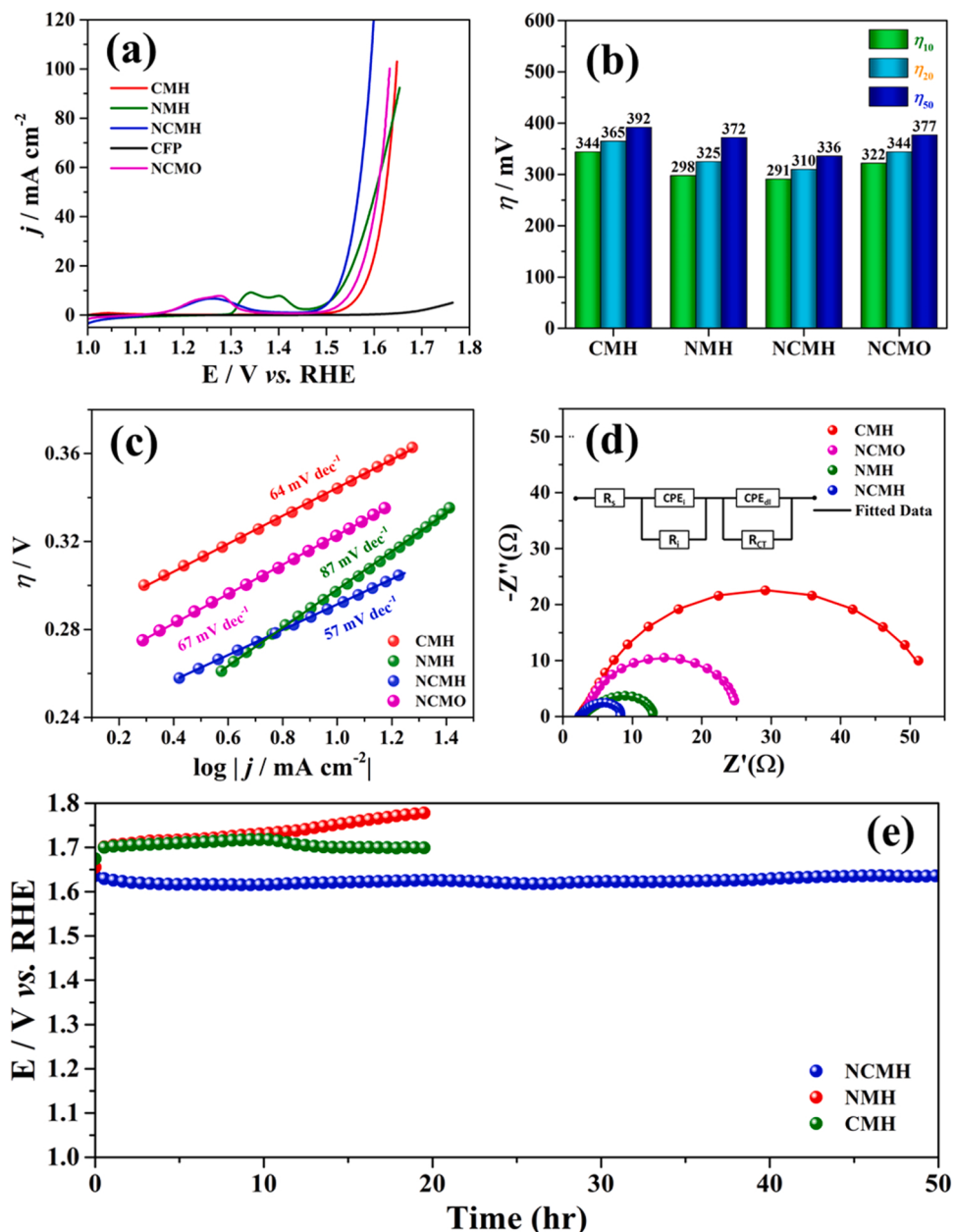


Fig. 4. (a) LSV curves with iR -correction at 5 mV s^{-1} , (b) overpotential values at $10, 20$, and 50 mA cm^{-2} current densities, (c) Tafel plots, and (d) Nyquist plots at 1.521 V (equivalent circuit at inset) of NMH, CMH, NCMH, and NCMO. (e) CP curves at 50 mA cm^{-2} of NMH, CMH, and NCMH.

previously reported similar OER electrocatalysts, such as NiMo hydrates@Pt-0.03 (399 mV @ 50 mA cm^{-2}), [19] NF/H-CoMoO₄ nanoplates (295 mV @ 10 mA cm^{-2}), [18] NiMoO₄ nanorods (340 mV @ 10 mA cm^{-2}), [17] CoNiMo oxide nanosheets (363 mV @ 10 mA cm^{-2}), [15] Ni_{0.75}Mo_{0.25} nanosheets/CC (330 mV @ 10 mA cm^{-2}), [51] and CoMoO₄-NiMoO₄ nanotubes (300 mV @ 10 mA cm^{-2}) [22].

The Tafel slope is a useful parameter for understanding kinetic pathways and determining the rate-determining step (RDS) of electrocatalytic reactions. The Tafel plot was derived from the iR -corrected LSV curves for NMH, CMH, NCMH, and NCMO (Fig. 4c), with the lowest Tafel slope observed for NCMH (57 mV dec^{-1}), indicating relatively faster OER kinetics in 1 M KOH. The Tafel analysis of NCMH was consistent with its OER performance; however, the Tafel slope values were inconsistent with the OER activities of NMH and CMH. This inconsistency could be related to the LSV curves of NMH and CMH, in which the OER performance of NMH deteriorated compared with that of

CMH in the higher overpotential region. Thus, in all probability, the inferior performance of NMH at high anodic potentials could account for its higher Tafel slope than that of CMH. Furthermore, Tafel slope of $\sim 57 \text{ mV dec}^{-1}$ indicates the adsorption of OH on electrode surface and formation of M-OH as the RDS for NCMH. [52].

To identify the charge transfer kinetics, EIS analyses of NMH, CMH, NCMH, and NCMO were performed at 1.521 V (vs. RHE); the recorded Nyquist plots are presented in Fig. 4d. Subsequently, the charge transfer resistance (R_{CT}) values of the prepared samples were derived by fitting the Nyquist plots to the equivalent circuit (inset of Fig. 4d). The calculated R_{CT} values for NMH, CMH, NCMH, and NCMO were $\sim 6.18, 48.99, 4.49$, and 20.29Ω , respectively. These findings clearly indicate that CMH shows very poor charge transfer kinetics, whereas NMH exhibits a much faster rate of charge transfer. NCMO also demonstrates sluggish charge transfer kinetics, which could be attributed to formation of heterostructure due to phase separation as observed from its XRD pattern (Fig. S9). Interestingly, a significant improvement in the electrical

conductivity was evident from the lowest R_{CT} value of NCMH. This can be ascribed to the electronic structure modulations of Ni and Co, present in NCMH, owing to the synergistic interaction, as observed earlier from the XPS analyses. [53] Thus, NCMH demonstrated the best charge transfer kinetics among the prepared materials. The C_{dl} value can be considered a direct measure of the ECSA [50] and CV measurements were carried out to determine the C_{dl} in the potential region of -0.15 to -0.05 V vs. Ag/AgCl. Multiple CV cycles (~ 50 cycles) was performed to get stable voltammograms followed by CVs at varied scan rates ($10\text{--}50\text{ mV s}^{-1}$). The reference point of current density appears to be close to zero with slight deviation (Fig. S10a-c), which may be due to dissimilar charging or discharging current densities as a result of the topographical complexities of working electrodes and interfaces. [54] In view of this, the difference between current densities of anodic and cathodic scans at -0.1 V are plotted against the scan rates to get $2 C_{dl}$ from the slope (Fig. S10d). Further, the C_{dl} values were determined to be ~ 2.72 , 2.37 , and 0.66 mF cm^{-2} for NMH, CMH, and NCMH, respectively. NCMH showed the highest C_{dl} (2.72 mF cm^{-2}) among the prepared samples, indicating the availability of a greater number of active sites compared to the other samples. Furthermore, fast removal of the generated oxygen gas bubbles is necessary to obtain better accessibility of the active sites and higher hydrophilicity/aerophobicity of the electrode surface is expected. [55] Contact angle measurements indicated that NCMH is more hydrophilic/aerophobic than NMH (Fig. S7). Consequently, the rapid release of oxygen bubbles and better mass transport properties could be related to the high oxygen-evolving ability of the NCMH.

Long-term stability is considered a critical parameter for the practical application of anode materials in water electrolysis. [56] In this regard, CP measurements were performed for NMH, CMH, and NCMH at 50 mA cm^{-2} to evaluate their long-term stability. The corresponding potential-time curves (Fig. 4e) illustrate the outstanding long-term stability of NCMH for 50 h with consistent OER performance. It is noted that NMH showed continuous degradation in OER activity and very poor stability throughout the measurement for 20 h . In contrast, the CMH exhibited an initial increase in the potential during the first 10.4 h , and then decreased until reaching 13.6 h , at which point the potential change stabilized for the remainder of the 20 h measurement. The relatively superior long-term stability of CMH compared with that of NMH is evident from the corresponding CP curves. Interestingly, by combining both Ni and Co in a single-crystal lattice in NCMH, excellent long-term performance and a low potential requirement to reach 50 mA cm^{-2} were achieved. These observations clearly infer the role of synergistic contribution of Ni and Co in NCMH for enhancing its OER performance and durability in 1 M KOH . Furthermore, LSV curves were recorded for NCMH to compare the changes in η_{10} before and after the CP analysis. A negligible increase ($\sim 5\text{ mV}$) in the η_{10} value of NCMH after electrolysis for 50 h at a high anodic current density (50 mA cm^{-2}) was observed (Fig. S11).

In addition, post-OER analysis of NCMH was carried out using FESEM, Raman spectroscopy, and XPS to characterize the morphological and structural changes. The FESEM images (Fig. S12) show that the rod-like morphology of NCMH was conserved after prolonged water electrolysis. However, hexagonal nanoplatelets were identified in the high-magnification FESEM image (Fig. S12b). This can be attributed to the oxidative surface reconstruction of NCMH during the OER with 1 M KOH . Such in situ reconstruction of transition metal oxides to (oxy)hydroxides during the OER is well documented in the literature. [28] To confirm this speculation, Raman and XPS were used to probe the structural evolution during the OER. The Raman spectrum of pristine NCMH compared to that after the OER (Fig. S13) showed that the stretching ($\text{Mo}=\text{O}$) and bending ($\text{O}-\text{Mo}-\text{O}$) vibrational modes of $[\text{MoO}_4]^{2-}$ unit completely disappeared after the OER, indicating leaching of Mo in the alkaline medium under OER conditions. In contrast, two new peaks appeared at $\sim 454\text{ cm}^{-1}$ and 537 cm^{-1} with a broad shoulder in the Raman spectrum of NCMH after the OER. These new peaks can be

assigned to the in situ formation of mixed-phase $\text{NiOOH}\text{-CoOOH}\text{-CoO}_2$ under the oxidative potential of the OER in alkaline media. [57,58] These in situ generated NiCo (oxy)hydroxides were therefore assigned as the real active species for the OER. A similar phenomenon involving Mo dissolution and the evolution of highly active (oxy)hydroxides has also been reported for metal molybdates. [59–62] Further, XPS analysis of NCMH after the OER is displayed in Fig. S14. The comparison of the before and after XPS survey spectra of NCMH also confirmed Mo leaching due to the disappearance of Mo peaks. In addition, Ni 2p and Co 2p high-resolution spectra indicated that the $\text{Ni}^{2+}/\text{Ni}^{3+}$ and $\text{Co}^{2+}/\text{Co}^{3+}$ atomic ratios (considering the $2\text{p}_{3/2}$ peak only) in after OER sample were changed from 2.53 to 0.38 and from 2.04 to 0.37 , respectively, in comparison to the pristine NCMH. This clearly suggests a large increase in the proportion of M^{3+} ($\text{M} = \text{Ni, Co}$) states, which further supports the oxidative reconstruction of NCMH to NiCo (oxy)hydroxide during the OER. Notably, Mo dissolution did not affect the OER performance of NCMH, as observed from the before and after durability LSV curves.

3.3. Density Functional Theory (DFT) Calculations

3.3.1. Surface Structure Optimization

First-principles DFT calculations were used to probe the interfacial chemistry and mechanistic pathways of the OER for NMH, CMH, and NCMH (see the Supplementary Information for the detailed computational methodology). XPS and FTIR analyses indicated enrichment of surface hydroxyl functionalities in NCMH owing to substitutional Co doping in NMH and boosted OER performance was also noted for such hydroxyl rich NCMH. To further strengthen these inferences, structural aspects and OER energetics of the hydrated catalysts were theoretically investigated using the hydrate DFT models instead of metal (oxy)hydroxides. The optimized bulk NCMH structure, as shown in Fig. S15a, demonstrated 010 facet as the most stable surface with high intensity (100%) in the simulated XRD pattern from VESTA [63] software as represented in Fig. S15b. In addition, Ratha et al. [64] extensively studied bifunctional activity toward oxygen evolution and supercapacitor using first-principles calculation using 010 facet of α and $\beta\text{-NiMoO}_4$ structure. Moreover, surface seems to be oxygen rich as Mo atom shows tetrahedral coordination with the neighboring oxygen atoms. Thus, the 010 facet was considered for the DFT calculations. Considering the size of the adsorbates, the catalyst surface could be properly modeled by extending the distance to 13.56 \AA and 9.25 \AA for the x - and y -axes, respectively, and a vacuum space of 20 \AA was set on the z -axis to minimize periodic image interactions in the neighboring cells. The $(2\times 1)\text{ NMH(010)}$, CMH(010) , and NCMH(010) surfaces were set to consist three layers, and each layer composed of four Mo and 16 O atoms along with four Ni for NMH, four Co for CMH, and two Ni and two Co atoms for NCMH, where the bottom layer was fixed and the top two layers were relaxed, as shown in Fig. S16. Moreover, we tried two possible bulk NCMH configurations (1 and 2) and their corresponding surface models are shown in Fig. S17, in which Co atoms were substituted at two different places. In the case of configuration 1 (Fig. S17c), the Co atoms were placed in the sublayer (layer 2) and in the configuration 2 (Fig. S17d), the Co atoms were placed in all the three layers evenly. The configuration 2 showed the most stable surface generation with 2 Co and 2 Ni atoms exposed on the top surface. Thus, it was used for our present study to evaluate the OER process.

To identify the active sites on NCMH(010) surface, we adsorbed OH^* on three different sites such as Ni-top, Co-top, and O-top followed by calculating the adsorption energies. The Mo sites are not available on the surface owing to their tetrahedral coordination with the adjacent O atoms. Ni-top site of NCMH(010) surface showed the most stable active site with an adsorption energy of -1.195 eV than Co-top and O-top sites (Fig. S18a). In addition, comparative free energy diagram of OER on Ni-top and O-top of NCMH(010) surface (Fig. S18b) were calculated to indicate the energy barrier of the potential-limiting step (PLS). The free energy barrier ($\Delta G = 2.68\text{ eV}$) for the conversion of $(^*\text{O} \rightarrow *_{\text{OOH}})$ on Ni-

top sites was significantly higher than that of the O-top sites ($\Delta G = 1.80$ eV). Therefore, O-top could be considered as the preferred sites for OER on NCMH(010) surface.

3.3.2. OER Mechanism on the NMH(010), CMH(010), and NCMH(010) Surfaces

The mechanism of the OER for the NMH(010), CMH(010), and NCMH(010) surfaces was studied in detail according to the following four electron proton transfer steps with OH, O, and OOH intermediates. [65] The proposed 4e⁻ OER mechanism with adsorbed species H₂O*, OH*, O*, OOH*, and O_{2(g)} on the NMH(010), CMH(010), and NCMH(010) surfaces are shown in Figs. S19, S20, and 5a, respectively; the OER pathway is as follows [66]: Eqs. (1–4), where the asterisks (*) and (g) indicate adsorbed and gas-phase species, respectively.



A comparative OER free energy diagram of the NMH(010), CMH

(010), and NCMH(010) surfaces is shown in Fig. 5b. In the case of the NMH(010) surface, the ΔG_1 step (H₂O* → OH*) shows maximum energy uphill than the rest of the OER steps, indicating that the energy barrier of the PLS is 2.21 eV. Similarly, in case of the CMH(010) and NCMH(010) surface, the ΔG_3 step (O* → OOH*) shows an maximum energy uphill with the energy barrier of the PLS of 2.21 and 1.80 eV, respectively. Based on the overall OER free energy comparison, NCMH exhibited relatively stable surface than the rest with the minimum PLS of 1.80 eV. Thus, the presence of Co with Ni surface in the NCMH catalyst serves a key role in enhancing the OER efficiency. The computed PLS results demonstrate that the presence of Co in the NCMH catalyst ultimately plays a key role in enhancing the OER efficiency by relatively strengthening the OH* adsorption on NCMH. Table S1 summarizes the adsorption energies of the OER intermediates and shows that the NCMH(010) surface outperforms the NMH(010) surface; in particular, the adsorption energies of OH (~−0.112 eV) and O (0.949 eV) in NCMH are relatively stronger than those in NMH (0.410 and 2.472 eV, respectively), whereas the rest of the adsorbates showed similar adsorption strengths on both surfaces. [23].

3.3.3. Fundamental Understanding on the Enhanced OER Mechanism

The enhanced OER efficiency of the NCMH catalyst can be attributed to an increase in OH adsorption strength due to the addition of Co to

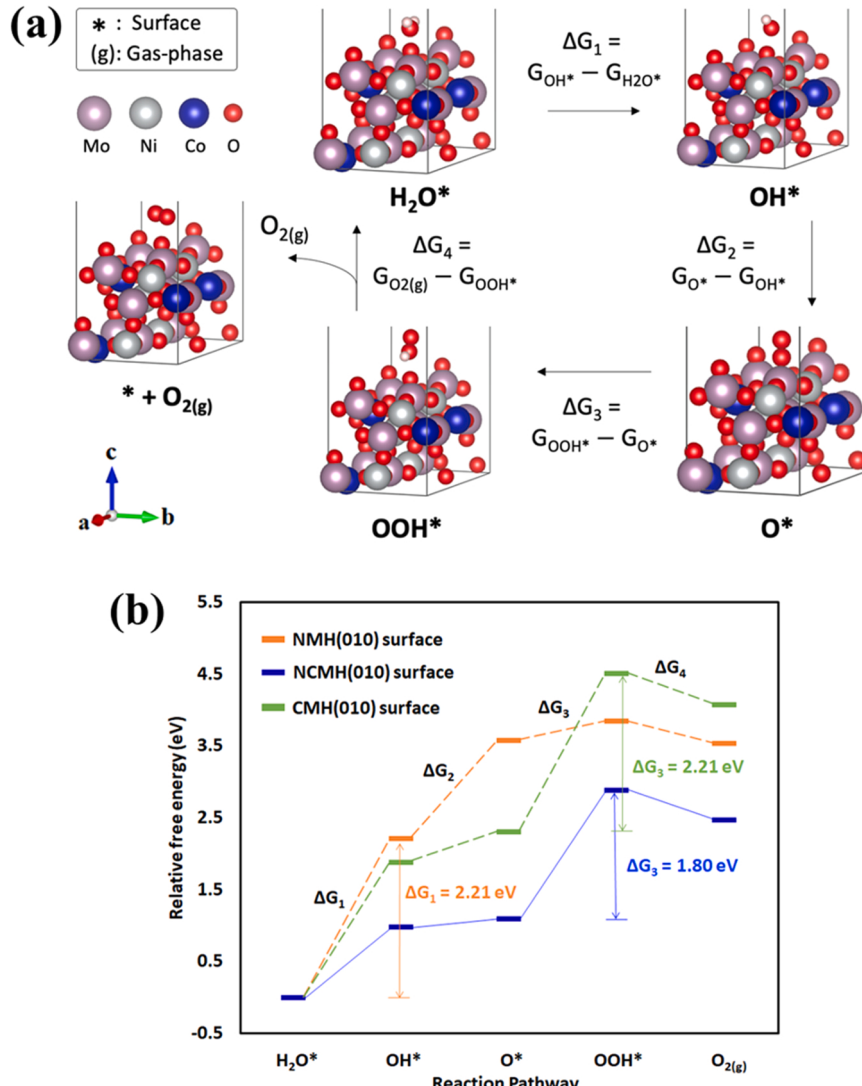


Fig. 5. (a) Proposed 4e⁻ OER mechanism with optimized OER intermediates of H₂O*, OH*, O*, and OOH*, and the final product of O_{2(g)} on the NCMH(010) surface. ΔG represents the reaction Gibbs free energy. (b) Relative free energy diagram of the OER on the NMH(010), CMH(010), and NCMH(010) surfaces.

NMH as a substitutional dopant. To understand the electron rearrangement in the NCMH catalyst due to the Co dopant, Bader charge and excess Bader charge analyses (i.e., Bader charge difference upon Co incorporation on a pristine surface; positive and negative signs represent charge gain and loss, respectively, upon substitutional doping) were conducted for the pristine catalyst surfaces. [67–69] Table S2 shows the excess Bader charges of the NCMH(010) surface, indicating that substitutional doping of Co allows the NCMH atoms to receive electron charge from Co due to the relatively smaller electronegativity of Co compared to those of the other atoms Co = 1.88, Ni = 1.91, Mo = 2.16, O = 3.44, Pauling scale). This suggests that the presence of Co on the NCMH surface causes a significant electron density redistribution that can affect the interactions between adsorbates and the catalyst surface.

Electron density redistribution due to substitutional doping of Co increased the electron density of NCMH surface oxygen atoms and increased the non-uniformity of oxygen electron density. Fig. 6 depicts the Bader charge values of the NMH and NCMH surface atoms. Although the average Bader charge values of the four oxygen atoms to which the OH molecules are adsorbed are similar (6.581e and 6.587e for NMH and NCMH, respectively), their standard deviations differ (0.036e and 0.059e for NMH and NCMH, respectively). In other words, the non-uniformity of the oxygen electron density on the NCMH surface was larger than that of NMH, which may be more favorable for OH adsorption. As the OH molecule has a partially negative O^{δ-} and a partially positive H^{δ+}, the partial positive charge on H may be attracted more favorably by the larger negative charge on the NCMH catalyst surface. Overall, it was confirmed that the NCMH(010) surface shows enhanced OER activity with a lower PLS compared to the NMH(010) surface, which also supports and validates the experimental prediction of superior electrocatalytic activity on hydrated nickel cobalt molybdate. In addition, in the bulk crystal structure of NMH, oxygen gains electrons from both Ni and Mo (the electron transfer direction is indicated by arrows ①–④ in Fig. 6) owing to its relatively large electronegativity. When Co exists instead of Ni in NCMH, more electrons accumulate on oxygen owing to the smaller electronegativity of Co compared to Ni.

3.4. AEM Water Electrolyzer Performance

To evaluate the practical applicability of the prepared OER electrocatalyst in water electrolysis systems, an AEM electrolyzer was assembled and the detailed process is provided in the [Supplementary Information](#). NCMH was used as the anode for OER in the AEM

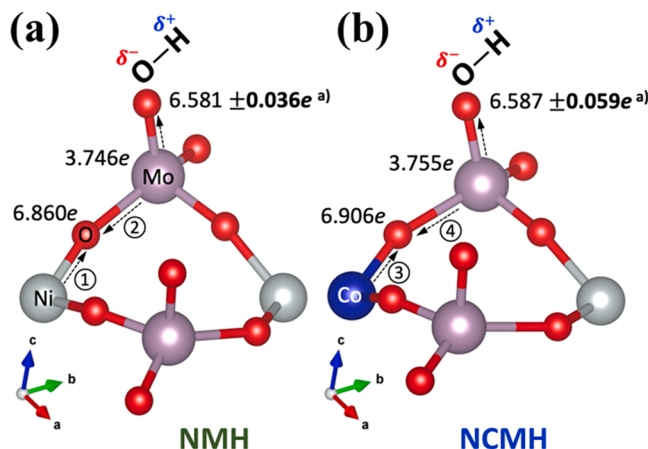


Fig. 6. Bader charges of the (a) NMH and (b) NCMH surface atoms to which an OH molecule is adsorbed. Superscript a) refers to the average and standard deviation of the Bader charge values of the four oxygen atoms on the surface. Arrows indicate the direction of electron flow due to the difference in electronegativity of atoms.

electrolyzer, the configuration of which is illustrated in Fig. 7a. For comparison, the commercially available benchmark OER electrocatalyst, IrO₂ was also used as anode. The Pt/C, known to be the best HER electrocatalyst, was employed as the cathode to minimize the polarization loss due to HER,. [70] The polarization curves of the NCMH and IrO₂ catalyzed AEM electrolyzers were estimated by the cell voltage at fixed current densities (Fig. 7b). The performance of the electrolyzer equipped with NCMH was higher than that of IrO₂ in all current regions. Specifically, to achieve a current density of 1.0 A cm⁻², the AEM electrolyzer required a 1.82 V_{cell} (NCMH) and 1.93 V_{cell} (IrO₂). The cell efficiencies of the AEM electrolyzer, at 0.5 A cm⁻² current density, were calculated to be ~74.57% (NCMH) and 71.55% (IrO₂). The cell efficiency and cell voltage at 1.0 A cm⁻² are summarized in Fig. 7c. Thus, it was confirmed that the AEM electrolyzer catalyzed by NCMH outperformed the AEM electrolyzer catalyzed by the precious metal electrocatalyst (IrO₂).

To further analyze the impact of the electrocatalyst on the AEM electrolyzer, EIS analysis was performed and Nyquist plots were obtained, as shown in Fig. 7d. The high-frequency resistance (HFR) is the intercept of the real impedance axis in the Nyquist plots, which is related to the ohmic resistance (η_{ohm}) of the AEM electrolyzer. The ohmic resistance is the sum of the electronic and ionic resistances of AEM electrolyzer. [71,72] The HFR values were 0.027 Ω (IrO₂) and 0.028 Ω (NCMH), indicating that the AEM electrolyzer catalyzed by IrO₂ has a lower resistance than that of NCMH. It was observed that the AEM electrolyzer equipped with NCMH had a slightly higher ohmic loss as the current density increased due to the difference in the HFR (Fig. S21). Specifically, the difference in the cell voltage at 1.0 A cm⁻² was negligible (~10 mV). The radius of the semicircle in the Nyquist plot indicates the polarization resistance of the AEM electrolyzer; [6] the radius of the AEM electrolyzer prepared with NCMH was smaller than that prepared with IrO₂, indicating better kinetics.

To analyze the difference in polarization resistance, we calculated the activation loss (η_{act}) of the AEM electrolyzer (Fig. 7e). The activation loss of AEM electrolyzer equipped with NCMH was significantly lower than that of IrO₂. In general, a highly active electrocatalyst improves the performance of AEM electrolyzer by reducing activation loss. [71] This means that our sample composed of non-precious metals has better kinetics than IrO₂ in the AEM electrolyzer. The durability of AEM electrolyzer catalyzed by NCMH was tested at a current density of 0.5 A cm⁻² for 58 h, as shown in Fig. 7f. The cell voltage increased slightly over time, and the cell degradation rate was approximately 1.0 mV h⁻¹.

During the durability test, the Faraday efficiency was calculated by measuring the amount of hydrogen gas generated. The theoretical hydrogen production rate at 0.5 A cm⁻² is approximately 0.058 mL s⁻¹ cm⁻². The actual H₂ production rate of the AEM electrolyzer was measured to be about 0.057 mL s⁻¹ cm⁻², which was very close to the theoretical value. This result indicated that the Faraday efficiency was approximately 98–99% (Fig. S22). In addition, our AEM electrolyzer was found to be comparable to the recently reported AEM electrolyzers (Fig. S23 and Table S3). These findings indicate that NCMH is an efficient and durable anode material for AEM water electrolysis.

4. Conclusions

1D NiCo molybdate hydrate nanostructured rods were successfully fabricated using a scalable one-step reflux technique. The partial substitution of Ni with Co in hydrated NiMoO₄ resulted in the formation of a single triclinic phase of NCMH due to the absence of any lattice mismatch and the close crystal radii of Ni and Co. Physicochemical characterizations indicated modulations of the electronic structure in NCMH owing to the collaborative interactions of Ni and Co. Interestingly, Co influenced the OH adsorption strength on the NCMH surface, leading to enrichment of the surface with hydroxyl groups. As a result, improved alkaline OER performance was noted for NCMH, with an

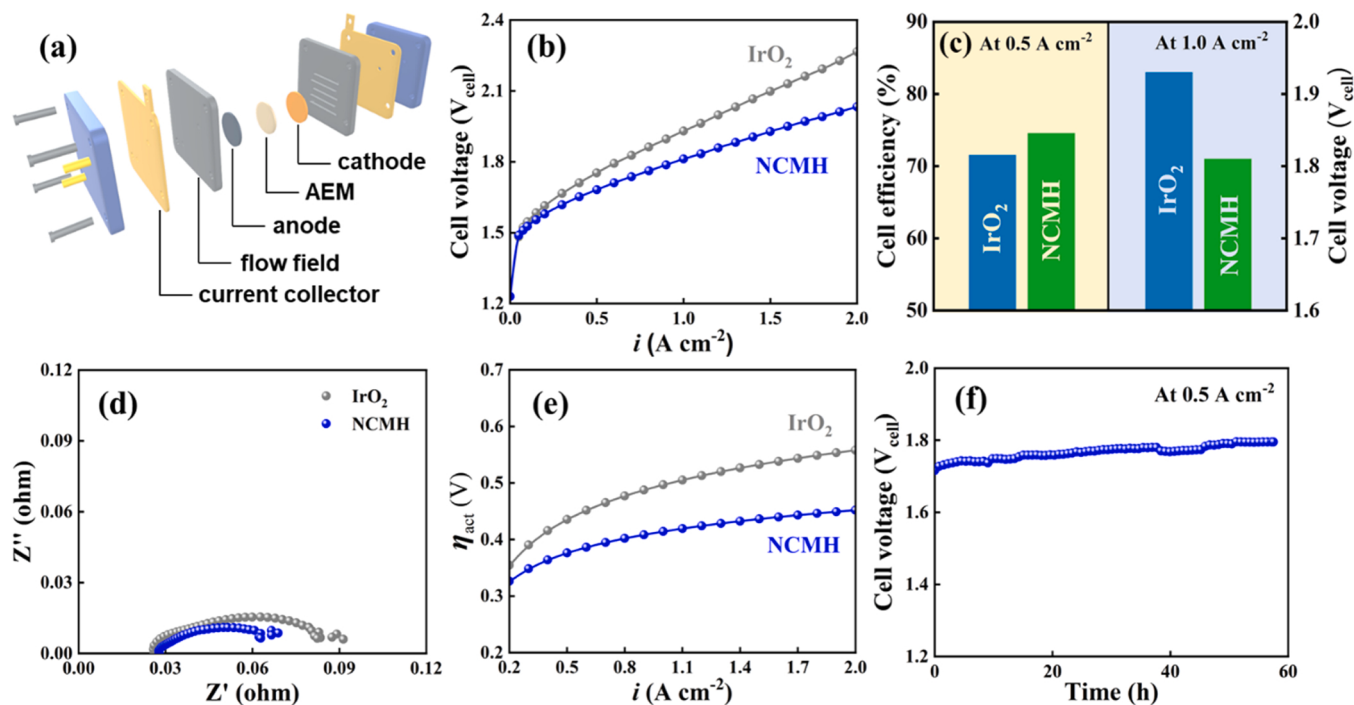


Fig. 7. Performance of AEM electrolyzer. (a) Schematic illustration of the AEM electrolyzer. (b) Polarization curves of AEM electrolyzers catalyzed by IrO_2 and NCMH. (c) Comparison of cell efficiencies at 0.5 A cm^{-2} and cell voltages at 1.0 A cm^{-2} . (d) Nyquist plots of the AEM electrolyzer at 0.5 A cm^{-2} . (e) Activation losses (η_{act}) of the AEM electrolyzer catalyzed by IrO_2 and NCMH. (f) Durability test of the AEM electrolyzer catalyzed by NCMH at 0.5 A cm^{-2} for 58 h.

overpotential of $\sim 291 \text{ mV}$ at 10 mA cm^{-2} and remarkable long-term stability for 50 h at 50 mA cm^{-2} in 1 M KOH . Furthermore, NCMH as the anode in the AEM water electrolyzer outperformed the commercial IrO_2 anode by exhibiting a current density of $\sim 1.0 \text{ A cm}^{-2}$ at $1.82 \text{ V}_{\text{cell}}$ with good cell efficiency ($\sim 74.57\%$). Therefore, the $\text{Ni}_{0.5}\text{Co}_{0.5}\text{MoO}_4$ hydrate nanostructured rods fabricated in one step are promising for use as an anode material in AEM electrolyzers and for making further strides toward a sustainable hydrogen fuel economy.

CRediT authorship contribution statement

Ayon Karmakar: Conceptualization, Methodology, Writing – original draft. **Thillai Govindaraja Senthamarai Kannan:** Software, Writing – original draft. **Erdenebayar Baasanjav:** Investigation, Formal analysis. **Parthasarathi Bandyopadhyay:** Methodology, Validation. **Bo Jin:** Data curation. **Yoo Sei Park:** Visualization, Supervision. **Dong-Hee Lim:** Supervision, Writing – review & editing. **Sang Mun Jeong:** Supervision, Writing – review & editing, Funding acquisition.

Declaration of Competing Interest

The authors declare that they have no known competing financial interests or personal relationships that could have appeared to influence the work reported in this paper.

Data Availability

Data will be made available on request.

Acknowledgements

This work was supported by Chungbuk National University BK21 program (2021).

Appendix A. Supporting information

Supplementary data associated with this article can be found in the online version at doi:10.1016/j.apcatb.2023.122504.

References

- [1] I. Dresselhaus, M.S. Thomas, M.S. Dresselhaus, I.L. Thomas, Alternative energy technologies, *Nature* 414 (2001) 332–337, <https://doi.org/10.1038/35104599>.
- [2] S. Chu, A. Majumdar, Opportunities and challenges for a sustainable energy future, *Nature* 488 (2012) 294–303, <https://doi.org/10.1038/nature11475>.
- [3] S. Ghosh, S. Barg, S.M. Jeong, K. (Ken) Ostrikov, Heteroatom-doped and oxygen-functionalized nanocarbons for high-performance supercapacitors, *Adv. Energy Mater.* 10 (2020) 2001239, <https://doi.org/10.1002/aenm.202001239>.
- [4] C. Hu, L. Zhang, J. Gong, Recent progress made in the mechanism comprehension and design of electrocatalysts for alkaline water splitting, *Energy Environ. Sci.* 12 (2019) 2620–2645, <https://doi.org/10.1039/c9ee01202h>.
- [5] J.S. Kim, B. Kim, H. Kim, K. Kang, Recent progress on multimetal oxide catalysts for the oxygen evolution reaction, *Adv. Energy Mater.* 8 (2018) 1–26, <https://doi.org/10.1002/aenm.201702774>.
- [6] J.E. Park, S.Y. Kang, S.H. Oh, J.K. Kim, M.S. Lim, C.Y. Ahn, Y.H. Cho, Y.E. Sung, High-performance anion-exchange membrane water electrolysis, *Electrochim. Acta* 295 (2019) 99–106, <https://doi.org/10.1016/J.ELECTACTA.2018.10.143>.
- [7] A.Y. Ganin, M.D. Symes, Towards the application of 2D metal dichalcogenides as hydrogen evolution electrocatalysts in proton exchange membrane electrolyzers, *Curr. Opin. Electrochem.* 34 (2022), 101001, <https://doi.org/10.1016/J.COULEC.2022.101001>.
- [8] Y.S. Park, J. Jeong, Y. Noh, M.J. Jang, J. Lee, K.H. Lee, D.C. Lim, M.H. Seo, W. B. Kim, J. Yang, S.M. Choi, Commercial anion exchange membrane water electrolyzer stack through non-precious metal electrocatalysts, *Appl. Catal. B Environ.* 292 (2021) 1–9, <https://doi.org/10.1016/j.apcatb.2021.120170>.
- [9] B. Wang, K. Zhao, Z. Yu, C. Sun, Z. Wang, N. Feng, L. Mai, Y. Wang, Y. Xia, In situ structural evolution of the multi-site alloy electrocatalyst to manipulate the intermediate for enhanced water oxidation reaction, *Energy Environ. Sci.* 13 (2020) 2200–2208, <https://doi.org/10.1039/D0EE00755B>.
- [10] A. Karmakar, H.S. Chavan, S.M. Jeong, J.S. Cho, Mixed transition metal carbonate hydroxide-based nanostructured electrocatalysts for alkaline oxygen evolution: status and perspectives, *Adv. Energy Sustain. Res.* 3 (2022) 2200071, <https://doi.org/10.1002/aesr.202200071>.
- [11] X. Lu, H. Xue, H. Gong, M. Bai, D. Tang, R. Ma, T. Sasaki, 2D layered double hydroxide nanosheets and their derivatives toward efficient oxygen evolution reaction, *Nano-Micro Lett.* 12 (2020) 86, <https://doi.org/10.1007/s40820-020-00421-5>.
- [12] F. Sun, G. Wang, Y. Ding, C. Wang, B. Yuan, Y. Lin, NiFe-Based metal–organic framework nanosheets directly supported on nickel foam acting as robust

- electrodes for electrochemical oxygen evolution reaction, *Adv. Energy Mater.* 8 (2018) 1800584, <https://doi.org/10.1002/AENM.201800584>.
- [13] J. Chen, G. Zhao, Y. Chen, K. Rui, H. Mao, S.X. Dou, W. Sun, Iron-doped nickel molybdate with enhanced oxygen evolution kinetics, *Chem. - A Eur. J.* 25 (2019) 280–284, <https://doi.org/10.1002/chem.201803844>.
- [14] A. Karmakar, K. Karthick, S.S. Sankar, S. Kumaravel, M. Ragunath, S. Kundu, Oxygen vacancy enriched NiMoO₄nanorods: Via microwave heating: a promising highly stable electrocatalyst for total water splitting, *J. Mater. Chem. A* 9 (2021) 11691–11704, <https://doi.org/10.1039/dta02165f>.
- [15] B. Ren, D. Li, Q. Jin, H. Cui, C. Wang, In-situ tailoring cobalt nickel molybdenum oxide components for overall water-splitting at high current densities, *ChemElectroChem* 6 (2019) 413–420, <https://doi.org/10.1002/celc.201801386>.
- [16] J. Wang, L. Li, L. Meng, L. Wang, Y. Liu, W. Li, W. Sun, G. Li, Morphology engineering of nickel molybdate hydrate nanoarray for electrocatalytic overall water splitting: From nanorod to nanosheet, *RSC Adv.* 8 (2018) 35131–35138, <https://doi.org/10.1039/c8ra07323f>.
- [17] X. Zhao, J. Meng, Z. Yan, F. Cheng, J. Chen, Nanostructured NiMoO₄ as active electrocatalyst for oxygen evolution, *Chin. Chem. Lett.* 30 (2019) 319–323, <https://doi.org/10.1016/j.cclet.2018.03.035>.
- [18] K. Chi, T. Tian, Q. Wang, Z. Zhang, X. Zhang, Y. Zhang, F. Jing, Q. Lv, W. Yao, F. Xiao, S. Wang, Oxygen vacancies engineered CoMoO₄ nanosheet arrays as efficient bifunctional electrocatalysts for overall water splitting, *J. Catal.* 381 (2020) 44–52, <https://doi.org/10.1016/j.jcat.2019.10.025>.
- [19] Y. Guan, Y. Liu, Pt modified Ni-Mo-based hydrates as bifunctional electrocatalysts for overall water splitting, *N. J. Chem.* 45 (2021) 16313–16318, <https://doi.org/10.1039/dnj02046c>.
- [20] I. Shakir, M. Sarfraz, U.A. Rana, M. Nadeem, M.A. Al-Shaikh, Synthesis of hierarchical porous spinel nickel cobaltite nanoflakes for high performance electrochemical energy storage supercapacitors, *RSC Adv.* 3 (2013) 21386–21389, <https://doi.org/10.1039/c3ra43973a>.
- [21] A. Karmakar, S.K. Srivastava, Interconnected copper cobaltite nanochains as efficient electrocatalysts for water oxidation in alkaline medium, *ACS Appl. Mater. Interfaces* 9 (2017) 22378–22387, <https://doi.org/10.1021/acsmi.7b03029>.
- [22] Z. Yin, Y. Chen, Y. Zhao, C. Li, C. Zhu, X. Zhang, Hierarchical nanosheet-based CoMoO₄-NiMoO₄ nanotubes for applications in asymmetric supercapacitors and the oxygen evolution reaction, *J. Mater. Chem. A* 3 (2015) 22750–22758, <https://doi.org/10.1039/c5ta05678k>.
- [23] Z. Wang, J. Chen, E. Song, N. Wang, J. Dong, X. Zhang, P.M. Ajayan, W. Yao, C. Wang, J. Liu, J. Shen, M. Ye, X. Zhang, P.M. Ajayan, W. Yao, C. Wang, J. Liu, J. Shen, M. Ye, Manipulation on active electronic states of metastable phase β -NiMoO₄ for large current density hydrogen evolution, *Nat. Commun.* 12 (2021) 1–10, <https://doi.org/10.1038/s41467-021-26256-1>.
- [24] D. Chu, X. Zhao, B. Xiao, A. Libanori, Y. Zhou, L. Tan, H. Ma, H. Pang, X. Wang, Y. Jiang, J. Chen, Nickel/Cobalt molybdate hollow rods induced by structure and defect engineering as exceptional electrode materials for hybrid supercapacitor, *Chem. A Eur. J.* 27 (2021) 8337–8343, <https://doi.org/10.1002/chem.202100265>.
- [25] X. Zhao, X. Liu, B. Huang, P. Wang, Y. Pei, Hydroxyl group modification improves the electrocatalytic ORR and OER activity of graphene supported single and bi-metal atomic catalysts (Ni, Co, and Fe), *J. Mater. Chem. A* 7 (2019) 24583–24593, <https://doi.org/10.1039/c9ta08661g>.
- [26] Z. Chen, C.X. Kronawitter, I. Waluyo, B.E. Koel, Investigation of water dissociation and surface hydroxyl stability on pure and Ni-modified CoOOH by ambient pressure photoelectron spectroscopy, *J. Phys. Chem. B.* 122 (2018) 810–817, <https://doi.org/10.1021/acs.jpcb.7b06960>.
- [27] Y.S. Park, J. Yang, J. Lee, M.J. Jang, J. Jeong, W.S. Choi, Y. Kim, Y. Yin, M.H. Seo, Z. Chen, S.M. Choi, Superior performance of anion exchange membrane water electrolyzer: ensemble of producing oxygen vacancies and controlling mass transfer resistance, *Appl. Catal. B Environ.* 278 (2020), 119276, <https://doi.org/10.1016/j.apcatb.2020.119276>.
- [28] Q. Xu, L. Zhang, J. Zhang, J. Wang, Y. Hu, H. Jiang, C. Li, Anion exchange membrane water electrolyzer: electrode design, lab-scaled testing system and performance evaluation, *EnergyChem* 4 (2022), 100087, <https://doi.org/10.1016/j.enchem.2022.100087>.
- [29] M.J. Jang, S.H. Yang, M.G. Park, J. Jeong, M.S. Cha, S. Shin, K.H. Lee, Z. Bai, Z. Chen, J.Y. Lee, S.M. Choi, Efficient and durable anion exchange membrane water electrolysis for a commercially available electrolyzer stack using alkaline electrolyte, *ACS Energy Lett.* 7 (2022) 2576–2583, <https://doi.org/10.1021/acsenergylett.2c01049>.
- [30] K. Eda, Y. Kato, Y. Ohshiro, T. Sugitani, M.S. Whittingham, Synthesis, crystal structure, and structural conversion of Ni molybdate hydrate NiMoO₄.nH₂O, *J. Solid State Chem.* 183 (2010) 1334–1339, <https://doi.org/10.1016/j.jssc.2010.04.009>.
- [31] K. Eda, Y. Uno, N. Nagai, N. Sotani, M.S. Whittingham, Crystal structure of cobalt molybdate hydrate CoMoO₄.nH₂O, *J. Solid State Chem.* 178 (2005) 2791–2797, <https://doi.org/10.1016/j.jssc.2005.06.014>.
- [32] R.D. Shannon, Revised effective ionic radii and systematic studies of interatomic distances in halides and chalcogenides, *Acta Crystallogr. Sect. A* 32 (1976) 751–767, <https://doi.org/10.1107/S0567739476001551>.
- [33] D.K. Denis, X. Sun, J. Zhang, Y. Wang, L. Hou, J. Li, C. Yuan, Solid solution engineering of Co-Ni-based ternary molybdate nanorods toward hybrid supercapacitors and lithium-ion batteries as high-performance electrodes, *ACS Appl. Energy Mater.* 3 (2020) 3955–3965, <https://doi.org/10.1021/acsaem.0c00353>.
- [34] S. Anantharaj, S. Noda, Amorphous catalysts and electrochemical water splitting: an untold story of harmony, *Small* 16 (2020) 1905779, <https://doi.org/10.1002/smll.201905779>.
- [35] M. Liu, Y.-C. Luo, J.-W. Lang, L.-B. Kong, L. Kang, Co[_{0.56}]Ni[_{0.44}] Oxide nanoflake materials and activated carbon for asymmetric supercapacitor, *J. Electrochem. Soc.* 157 (2010) A1341–A1346, <https://doi.org/10.1149/1.3497298>.
- [36] H. Wan, J. Jiang, X. Ji, L. Miao, L. Zhang, K. Xu, H. Chen, Y. Ruan, Rapid microwave-assisted synthesis NiMoO₄-H₂O nanoclusters for supercapacitors, *Mater. Lett.* 108 (2013) 164–167, <https://doi.org/10.1016/j.matlet.2013.06.099>.
- [37] S.T. Xiao, S.M. Wu, Y. Dong, J.W. Liu, L.Y. Wang, L. Wu, Y.X. Zhang, G. Tian, C. Janiak, M. Shalom, Y.T. Wang, Y.Z. Li, R.K. Jia, D.W. Bahnamann, X.Y. Yang, Rich surface hydroxyl design for nanostructured TiO₂ and its hole-trapping effect, *Chem. Eng. J.* 400 (2020) 1–8, <https://doi.org/10.1016/j.cej.2020.125909>.
- [38] M.J. Barmi, M.M. Sundaram, Role of polymeric surfactant in the synthesis of cobalt molybdate nanospheres for hybrid capacitor applications, *RSC Adv.* 6 (2016) 36152–36162, <https://doi.org/10.1039/C6RA02628A>.
- [39] G. Kianpour, M. Salavati-Niasari, H. Emadi, Precipitation synthesis and characterization of cobalt molybdates nanostructures, *Superlattices Micro* 58 (2013) 120–129, <https://doi.org/10.1016/j.spmi.2013.01.014>.
- [40] K.-S. Park, S.-D. Seo, H.-W. Shim, D.-W. Kim, Electrochemical performance of Ni_xCo_{1-x}MoO₄ (0 < x < 1) nanowire anodes for lithium-ion batteries, *Nanoscale Res. Lett.* 7 (2012) 35, <https://doi.org/10.1186/1556-276X-7-35>.
- [41] S.M.N. Jeghan, N. Kim, G. Lee, Mo-incorporated three-dimensional hierarchical ternary nickel-cobalt-molybdenum layer double hydroxide for high-efficiency water splitting, *Int. J. Hydrol. Energy* 46 (2021) 22463–22477, <https://doi.org/10.1016/j.ijhydene.2021.04.071>.
- [42] Z. Ma, H. Meng, M. Wang, B. Tang, J. Li, X. Wang, Porous Ni–Mo–S nanowire network film electrode as a high-efficiency bifunctional electrocatalyst for overall water splitting, *ChemElectroChem* 5 (2018) 335–342, <https://doi.org/10.1002/celc.201700965>.
- [43] D. Wang, Q. Li, C. Han, Q. Lu, Z. Xing, X. Yang, Atomic and electronic modulation of self-supported nickel-vanadium layered double hydroxide to accelerate water splitting kinetics, *Nat. Commun.* 10 (2019) 1–12, <https://doi.org/10.1038/s41467-019-11765-x>.
- [44] P. Thangavel, M. Ha, S. Kumaraguru, A. Meena, A.N. Singh, A.M. Harzandi, K. S. Kim, Graphene-nanoplatelets-supported NiFe-MOF: High-efficiency and ultra-stable oxygen electrodes for sustained alkaline anion exchange membrane water electrolysis, *Energy Environ. Sci.* 13 (2020) 3447–3458, <https://doi.org/10.1039/d0ee00877j>.
- [45] R. Jiang, D. Zhao, H. Fan, Y. Xie, M. Li, H. Lin, Z.S. Wu, Phosphorus doping and phosphates coating for nickel molybdate/nickel molybdate hydrate enabling efficient overall water splitting, *J. Colloid Interface Sci.* 606 (2022) 384–392, <https://doi.org/10.1016/j.jcis.2021.08.035>.
- [46] D.K. Denis, X. Sun, L. Hou, G. Chen, C. Yuan, Rate balance design and construction of a conductive Ni_{0.5}Co_{0.5}Mo_{0.4}Solid-solution microspherical superstructure toward advanced hybrid supercapacitors, *ACS Appl. Energy Mater.* 4 (2021) 9470–9478, <https://doi.org/10.1021/acsaelm.1c01664>.
- [47] T. Bhowmik, M.K. Kundu, S. Barman, CoFe layered double hydroxide supported on graphitic carbon nitrides: an efficient and durable bifunctional electrocatalyst for oxygen evolution and hydrogen evolution reactions, *ACS Appl. Energy Mater.* 1 (2018) 1200–1209, https://doi.org/10.1021/ACSAEM.7B00305/ASSET/IMAGES/LARGE/AE-2017-00305Z_0006.JPG.
- [48] H. Sun, X. Xu, Y. Song, W. Zhou, Z. Shao, Designing high-valence metal sites for electrochemical water splitting, *Adv. Funct. Mater.* 31 (2021) 2009779, <https://doi.org/10.1002/adfm.202009779>.
- [49] M.J. Jang, J. Yang, J. Lee, Y.S. Park, J.Y. Jeong, S.M. Park, J.Y. Jeong, Y. Yin, M. H. Seo, S.M. Choi, K.H. Lee, Superior performance and stability of anion exchange membrane water electrolysis: PH-controlled copper cobalt oxide nanoparticles for the oxygen evolution reaction, *J. Mater. Chem. A* 8 (2020) 4290–4299, <https://doi.org/10.1039/c9ta13137j>.
- [50] A. Karmakar, S.K. Srivastava, Hierarchically hollow interconnected rings of nickel substituted cobalt carbonate hydroxide hydrate as promising oxygen evolution electrocatalyst, *Int. J. Hydrol. Energy* 47 (2022) 22430–22441, <https://doi.org/10.1016/j.ijhydene.2022.05.062>.
- [51] R. Tong, Z. Sun, X. Wang, S. Wang, H. Pan, Network-Like Ni_{1-x}Mo_x nanosheets: multi-functional electrodes for overall water splitting and supercapacitor, *ChemElectroChem* 6 (2019) 1338–1343, <https://doi.org/10.1002/celc.201801725>.
- [52] X. Liu, Z. Chang, L. Luo, T. Xu, X. Lei, J. Liu, X. Sun, Hierarchical Zn x Co₃-xO₄ nanoarrays with high activity for electrocatalytic oxygen evolution, *Chem. Mater.* 26 (2014) 1889–1895, <https://doi.org/10.1021/cm4040903>.
- [53] N.I. Kim, Y.J. Sa, S.H. Cho, I. So, K. Kwon, S.H. Joo, J.Y. Park, Enhancing activity and stability of cobalt oxide electrocatalysts for the oxygen evolution reaction via transition metal doping, *J. Electrochem. Soc.* 163 (2016) F3020–F3028, <https://doi.org/10.1149/2.0031611jes>.
- [54] S. Anantharaj, P.E. Karthik, S. Noda, The significance of properly reporting turnover frequency in electrocatalysis research, *Angew. Chem. - Int. Ed.* 60 (2021) 23051–23067, <https://doi.org/10.1002/anie.202110352>.
- [55] M. Jiang, H. Wang, Y. Li, H. Zhang, G. Zhang, Z. Lu, X. Sun, L. Jiang, Superaerophilic RuO₂-based nanostructured electrode for high-performance chlorine evolution reaction, *Small* 13 (2017) 1602240, <https://doi.org/10.1002/smll.201602240>.
- [56] S. Anantharaj, P.E. Karthik, S. Sam Sankar, K. Sangeetha, P.E. Karthik, S. Kundu, Precision and correctness in the evaluation of electrocatalytic water splitting: revisiting activity parameters with a critical assessment, *Energy Environ. Sci.* 11 (2018) 744–771, <https://doi.org/10.1039/c7ee03457a>.

- [57] Z. Chen, L. Cai, X. Yang, C. Kronawitter, L. Guo, S. Shen, B.E. Koel, Reversible structural evolution of NiCoO_xHy during the oxygen evolution reaction and identification of the catalytically active phase, *ACS Catal.* 8 (2018) 1238–1247, <https://doi.org/10.1021/acscatal.7b03191>.
- [58] X. Yang, H. Zhang, B. Yu, Y. Liu, W. Xu, Z. Wu, An UNveiled Electrocatalysis Essence of Nico Hydroxides through in Situ Raman Spectroscopy for Urea Oxidation, *Energy Technol.* 10 (2022) 1–10, <https://doi.org/10.1002/ente.202101010>.
- [59] S. Ganguli, S. Ghosh, S. Das, V. Mahalingam, Inception of molybdate as a “pore forming additive” to enhance the bifunctional electrocatalytic activity of nickel and cobalt based mixed hydroxides for overall water splitting, *Nanoscale* 11 (2019) 16896–16906, <https://doi.org/10.1039/c9nr05142b>.
- [60] R.N. Dürr, P. Maltoni, H. Tian, B. Jousselme, L. Hammarström, T. Edvinsson, From NiMoO₄to γ -NiOOH: detecting the active catalyst phase by time resolved in situ and operando raman spectroscopy, *ACS Nano* 15 (2021) 13504–13515, <https://doi.org/10.1021/acsnano.1c04126>.
- [61] A. Rajput, M.K. Adak, B. Chakraborty, Intrinsic lability of NiMoO₄ to excel the oxygen evolution reaction, *Inorg. Chem.* 61 (2022) 11189–11206, <https://doi.org/10.1021/acs.inorgchem.2c01167>.
- [62] G. Solomon, A. Landström, R. Mazzaro, M. Jugovac, P. Moras, E. Cattaruzza, V. Morandi, I. Concina, A. Vomiero, NiMoO₄@Co₃O₄ core–shell nanorods: in situ catalyst reconstruction toward high efficiency oxygen evolution reaction, *Adv. Energy Mater.* 11 (2021) 2101324. (<https://onlinelibrary.wiley.com/doi/full/10.1002/aenm.202101324>).
- [63] K. Momma, F. Izumi, VESTA 3 for three-dimensional visualization of crystal, volumetric and morphology data, *J. Appl. Crystallogr.* 44 (2011) 1272–1276, <https://doi.org/10.1107/S0021889811038970/HTTP://JOURNALS.IUCR.ORG/SERVICES/PERMISSIONS.HTML>.
- [64] S. Ratha, A.K. Samantara, K.K. Singha, A.S. Gangan, B. Chakraborty, B.K. Jena, C. S. Rout, Urea-assisted room temperature stabilized metastable β -NiMoO₄: experimental and theoretical insights into its unique bifunctional activity toward oxygen evolution and supercapacitor, *ACS Appl. Mater. Interfaces* 9 (2017) 9640–9653, <https://doi.org/10.1021/acsami.6b16250>.
- [65] Z. Xu, J. Rossmeisl, J.R. Kitchin, A linear response DFT+U study of trends in the oxygen evolution activity of transition metal rutile dioxides, *J. Phys. Chem. C* 119 (2015) 4827–4833, https://doi.org/10.1021/JP511426Q/SUPPL_FILE/JP511426Q_SI_001.PDF.
- [66] Y. Jiao, Y. Zheng, M. Jaroniec, S.Z. Qiao, Design of electrocatalysts for oxygen- and hydrogen-involving energy conversion reactions, *Chem. Soc. Rev.* 44 (2015) 2060–2086, <https://doi.org/10.1039/c4cs00470a>.
- [67] R.F.W. Bader, A quantum theory of molecular structure and its applications, *Chem. Rev.* 91 (1991) 893–928, https://doi.org/10.1021/CR00005A013/ASSET/CRO0005A013.FP.PNG_V03.
- [68] Y.S. Han, C.M. Lee, C.M. Chon, J.A. Kwon, J.H. Park, Y.J. Shin, D.H. Lim, Enhanced oxidation resistance of NaBH₄-treated mackinawite (FeS): application to Cr(VI) and As(III) removal, *Chem. Eng. J.* 353 (2018) 890–899, <https://doi.org/10.1016/J.CEJ.2018.07.132>.
- [69] D.Y. Shin, Y.J. Shin, M.S. Kim, J.A. Kwon, D.H. Lim, Density functional theory-based design of a Pt-skinned PtNi catalyst for the oxygen reduction reaction in fuel cells, *Appl. Surf. Sci.* 565 (2021), 150518, <https://doi.org/10.1016/J.APSUSC.2021.150518>.
- [70] Q. Xu, S.Z. Oener, G. Lindquist, H. Jiang, C. Li, S.W. Boettcher, Integrated reference electrodes in anion-exchange-membrane electrolyzers: impact of stainless-steel gas-diffusion layers and internal mechanical pressure, *ACS Energy Lett.* 6 (2021) 305–312, <https://doi.org/10.1021/ACSENERGYLETT.0C02338/ASSET/IMAGES/LARGE/NZ0C02338.0006.JPG>.
- [71] Y.S. Park, F. Liu, D. Diercks, D. Braaten, B. Liu, C. Duan, High-performance anion exchange membrane water electrolyzer enabled by highly active oxygen evolution reaction electrocatalysts: synergistic effect of doping and heterostructure, *Appl. Catal. B Environ.* 318 (2022), 121824, <https://doi.org/10.1016/J.APCATB.2022.121824>.
- [72] Y.S. Park, J. Lee, M.J. Jang, J. Yang, J. Jeong, J. Park, Y. Kim, M.H. Seo, Z. Chen, S. M. Choi, High-performance anion exchange membrane alkaline seawater electrolysis, *J. Mater. Chem. A* 9 (2021) 9586–9592, <https://doi.org/10.1039/DOCA12336F>.